

Measurement of the Target-Normal Single-Spin Asymmetry in Deep-Inelastic Scattering from the Reaction ${}^3\text{He}^\uparrow(e, e')X$

J. Katich,^{1,2} X. Qian,^{3,4,5} Y. X. Zhao,⁶ K. Allada,⁷ K. Aniol,⁸ J. R. M. Annand,⁹ T. Averett,^{1,*} F. Benmokhtar,¹⁰ W. Bertozzi,¹¹ P.C. Bradshaw,¹ P. Bosted,¹ A. Camsonne,¹² M. Canan,¹³ G. D. Cates,¹⁴ C. Chen,¹⁵ J.-P. Chen,¹² W. Chen,³ K. Chirapatpimol,¹⁴ E. Chudakov,¹² E. Cisbani,^{16,17} J.C. Cornejo,⁸ F. Cusanno,^{16,17} M. M. Dalton,¹⁴ W. Deconinck,¹¹ C. W. de Jager,^{12,14} R. De Leo,¹⁸ X. Deng,¹⁴ A. Deur,¹² H. Ding,¹⁴ P. A. M. Dolph,¹⁴ C. Dutta,⁷ D. Dutta,¹⁹ L. El Fassi,^{13,20} S. Frullani,^{16,17} H. Gao,³ F. Garibaldi,^{16,17} D. Gaskell,¹² S. Gilad,¹¹ R. Gilman,^{12,20} O. Glamazdin,²¹ S. Golge,¹³ L. Guo,²² D. Hamilton,⁹ O. Hansen,¹² D. W. Higinbotham,¹² T. Holmstrom,²³ J. Huang,¹¹ M. Huang,³ H. F. Ibrahim,²⁴ M. Iodice,²⁵ X. Jiang,^{20,22} G. Jin,¹⁴ M. K. Jones,¹² A. Kelleher,¹ W. Kim,²⁶ A. Kolarkar,⁷ W. Korsch,⁷ J. J. LeRose,¹² X. Li,²⁷ Y. Li,²⁷ R. Lindgren,¹⁴ N. Liyanage,¹⁴ E. Long,²⁸ H.-J. Lu,⁶ D.J. Margaziotis,⁸ P. Markowitz,²⁹ S. Marrone,¹⁸ D. McNulty,³⁰ Z.-E. Meziani,³¹ R. Michaels,¹² B. Moffit,^{11,12} C. Muñoz Camacho,³² S. Nanda,¹² A. Narayan,¹⁹ V. Nelyubin,¹⁴ B. Norum,¹⁴ Y. Oh,³³ M. Osipenko,³⁴ D. Parno,¹⁰ J. C. Peng,³⁵ S. K. Phillips,²⁸ M. Posik,³¹ A. J. R. Puckett,^{11,22} Y. Qiang,^{3,12} A. Rakhman,³⁶ R. D. Ransome,²⁰ S. Riordan,¹⁴ A. Saha,^{12,†} B. Sawatzky,^{12,31} E. Schulte,²⁰ A. Shahinyan,³⁷ M. H. Shabestari,¹⁴ S. Širca,³⁸ S. Stepanyan,³⁹ R. Subedi,¹⁴ V. Sulkosky,^{11,12} L.-G. Tang,¹⁵ A. Tobias,¹⁴ G. M. Urciuoli,¹⁶ I. Vilardi,¹⁸ K. Wang,¹⁴ Y. Wang,³⁵ B. Wojtsekhowski,¹² X. Yan,⁶ H. Yao,³¹ Y. Ye,⁶ Z. Ye,¹⁵ L. Yuan,¹⁵ X. Zhan,¹¹ Y. Zhang,⁴⁰ Y.-W. Zhang,⁴⁰ B. Zhao,¹ X. Zheng,¹⁴ L. Zhu,^{15,35} X. Zhu,³ and X. Zong³

¹College of William and Mary, Williamsburg, VA 23187

²University of Colorado, Boulder, CO 80309

³Duke University, Durham, NC 27708

⁴Kellogg Radiation Laboratory, California Institute of Technology, Pasadena, CA, 91125

⁵Brookhaven National Laboratory, Upton, NY 11973

⁶University of Science and Technology of China, Hefei 230026, People's Republic of China

⁷University of Kentucky, Lexington, KY 40506

⁸California State University, Los Angeles, Los Angeles, CA 90032

⁹University of Glasgow, Glasgow G12 8QQ, Scotland, United Kingdom

¹⁰Carnegie Mellon University, Pittsburgh, PA 15213

¹¹Massachusetts Institute of Technology, Cambridge, MA 02139

¹²Thomas Jefferson National Accelerator Facility, Newport News, VA 23606

¹³Old Dominion University, Norfolk, VA 23529

¹⁴University of Virginia, Charlottesville, VA 22904

¹⁵Hampton University, Hampton, VA 23187

¹⁶INFN, Sezione di Roma, I-00161 Rome, Italy

¹⁷Istituto Superiore di Sanità, I-00161 Rome, Italy

¹⁸INFN, Sezione di Bari and University of Bari, I-70126 Bari, Italy

¹⁹Mississippi State University, Mississippi State, MS 39762

²⁰Rutgers, The State University of New Jersey, Piscataway, NJ 08855

²¹Kharkov Institute of Physics and Technology, Kharkov 61108, Ukraine

²²Los Alamos National Laboratory, Los Alamos, NM 87545

²³Longwood University, Farmville, VA 23909

²⁴Cairo University, Giza 12613, Egypt

²⁵INFN, Sezione di Roma3, I-00146 Rome, Italy

²⁶Kyungpook National University, Taegu 702-701, Republic of Korea

²⁷China Institute of Atomic Energy, Beijing, People's Republic of China

²⁸University of New Hampshire, Durham, NH 03824

²⁹Florida International University, Miami, FL 33199

³⁰University of Massachusetts, Amherst, MA 01003

³¹Temple University, Philadelphia, PA 19122

³²Université Blaise Pascal/IN2P3, F-63177 Aubière, France

³³Seoul National University, Seoul, 151-747, Republic of Korea

³⁴INFN, Sezione di Genova, I-16146 Genova, Italy

³⁵University of Illinois at Urbana-Champaign, Urbana, IL 61801

³⁶Syracuse University, Syracuse, NY 13244

³⁷Yerevan Physics Institute, Yerevan 375036, Armenia

³⁸University of Ljubljana, SI-1000 Ljubljana, Slovenia

³⁹Kyungpook National University, Daegu 702-701, Republic of Korea

⁴⁰Lanzhou University, Lanzhou 730000, Gansu, People's Republic of China

(Dated: October 29, 2018)

We report the first measurement of the target-normal single-spin asymmetry in deep-inelastic scattering from the inclusive reaction ${}^3\text{He}^\uparrow(e, e')X$ on a polarized ${}^3\text{He}$ gas target. Assuming time-reversal invariance, this asymmetry is strictly zero in the Born approximation but can be non-zero if two-photon-exchange contributions are included. The experiment, conducted at Jefferson Lab using a 5.89 GeV electron beam, covers a range of $1.7 < W < 2.9$ GeV, $1.0 < Q^2 < 4.0$ GeV² and $0.16 < x < 0.65$. Neutron asymmetries were extracted using the effective nucleon polarization and measured proton-to- ${}^3\text{He}$ cross section ratios. The measured neutron asymmetries are negative with an average value of $(-1.09 \pm 0.38) \times 10^{-2}$ for invariant mass $W > 2$ GeV, which is non-zero at the 2.89σ level. Our measured asymmetry agrees both in sign and magnitude with a two-photon-exchange model prediction that uses input from the Sivers transverse momentum distribution obtained from semi-inclusive deep-inelastic scattering.

PACS numbers: 25.30.Dh, 25.30.Fj, 24.70.+s, 21.10.Gv, 14.20.Dh, 29.25.Pj

The past decade has seen a resurrection of interest in two-photon exchange in electron-nucleon scattering. This is primarily due to the realization that inclusion of the two-photon-exchange amplitude can partially reconcile the discrepancy between the Rosenbluth separation and the polarization-transfer methods for extracting the Q^2 -dependence of the proton elastic form factor ratio, G_E^p/G_M^p [1–8]. As the precision of nucleon structure measurements improves, it is important to understand the dynamics of the two-photon-exchange processes. Assuming conservation of parity and time-reversal invariance, the target single-spin asymmetry (SSA) in (e, e') from a target polarized normal to the electron scattering plane is strictly zero at Born level [9], but can be non-zero when interference between one- and two-photon exchange processes is included (Fig. 1).

Consider the inelastic scattering of an unpolarized electron from a target nucleon with vector spin \vec{S} , oriented perpendicular (transversely polarized) to the incident electron 3-momentum \vec{k} , with normalization $|\vec{S}| = 1$. Requiring conservation of the electromagnetic current and parity, the differential cross section, $d\sigma$, for inclusive scattering is written as [9–11]

$$\begin{aligned} d\sigma(\phi_S) &= d\sigma_{UU} + \frac{\vec{S} \cdot (\vec{k} \times \vec{k}')}{|\vec{k} \times \vec{k}'|} d\sigma_{UT} \\ &= d\sigma_{UU} + d\sigma_{UT} \sin \phi_S, \end{aligned} \quad (1)$$

where \vec{k}' is the 3-momentum of the scattered electron, and $d\sigma_{UU}$ and $d\sigma_{UT}$ are the cross sections for an unpolarized electron scattered from an unpolarized and transversely polarized target, respectively. Our choice of coordinates is shown in Fig. 2 with the angle ϕ_S between the lepton plane and \vec{S} . The $+\hat{y}$ direction is parallel to the vector $\vec{k} \times \vec{k}'$ and corresponds to $\phi_S = 90^\circ$. We define the SSA as

$$A_{UT}(\phi_S) = \frac{d\sigma(\phi_S) - d\sigma(\phi_S + \pi)}{d\sigma(\phi_S) + d\sigma(\phi_S + \pi)} = A_y \sin \phi_S. \quad (3)$$

The quantity $A_y \equiv \frac{d\sigma_{UT}}{d\sigma_{UU}}$ can be extracted by measuring the ϕ_S -dependence of $A_{UT}(\phi_S)$, or by measuring the SSA for a target polarized normal to the lepton plane.

Considering only the one-photon-exchange amplitude, $\mathcal{M}_{1\gamma}$, we can write $d\sigma_{UU} \propto \mathcal{R}e(\mathcal{M}_{1\gamma}\mathcal{M}_{1\gamma}^*)$ and $d\sigma_{UT} \propto$

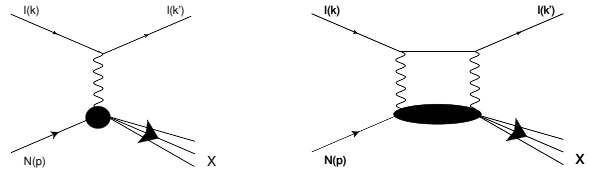


FIG. 1. Interference between one- and two-photon exchange in $N(e, e')$ allows the possibility of a non-zero target SSA. Here, l is the lepton with incident and outgoing 4-momenta k and k' , respectively. N is the nucleon with initial 4-momentum p .

$\mathcal{I}m(\mathcal{M}_{1\gamma}\mathcal{M}_{1\gamma}^*)$, where $\mathcal{R}e(\mathcal{I}m)$ stands for the real (imaginary) part. However time-reversal invariance requires that $\mathcal{M}_{1\gamma}$ be real and so at order α_{em}^2 , $d\sigma_{UU}$ can be non-zero but $d\sigma_{UT}$ must be zero. When one includes the (complex) two-photon-exchange amplitude, $\mathcal{M}_{2\gamma}$, the contribution to the asymmetry from one- and two-photon interference is $d\sigma_{UT} \propto \mathcal{I}m(\mathcal{M}_{1\gamma}\mathcal{M}_{2\gamma}^*)$ which can be non-zero at order α_{em}^3 . The two-photon exchange process forms a loop with the nucleon intermediate state and contains the full response of the nucleon (see Fig. 1).

An additional contribution to $d\sigma_{UT}$ at order α_{em}^3 may arise from interference between real photon emission (bremsstrahlung) by the electron and the hadronic system. Detailed discussions of these contributions are presented in Refs. [11–13].

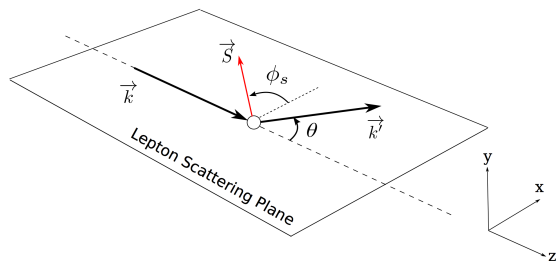


FIG. 2. Coordinate system used to define $A_{UT}(\phi_S)$.

There are no published measurements of A_y for the neutron. For protons, the first measurement of A_y^p was done in 1968 at CEA [14]. Electrons were scattered from

an alcohol/water target containing protons with an average polarization $\sim 20\%$. Three invariant photon-hadron masses were studied, $W = 1236, 1512$ and 1688 MeV, with $Q^2 = 0.2-0.7$ GeV². Results were consistent with zero at the 4×10^{-2} level. In 1969 a measurement at SLAC [15] was made using both e^- and e^+ scattering in the resonance region with $Q^2 = 0.4-1.0$ GeV². A butanol target provided protons with a polarization of $\sim 20\%$. Results were consistent with zero at the few $\times 10^{-2}$ level.

A theoretical calculation for A_y^p at $W = 1232$ MeV [10] treated the intermediate state as purely elastic and predicted $A_y^p \sim 0.75 \times 10^{-2}$ at $Q^2 = 0.6$ GeV².

The only measurement of A_y^p using deep-inelastic scattering (DIS) was made at DESY by the HERMES collaboration [16]. Both e^- and e^+ with energy 27.6 GeV were scattered from a polarized hydrogen target with average polarization $\sim 75\%$. Particles were detected over $0.007 < x_B < 0.9$, $0.25 < Q^2 < 20$ GeV² and $\phi_S = 0-2\pi$. Results for A_y^p for $Q^2 > 1$ GeV² are consistent with zero at the $\sim 10^{-3}$ level.

There are two parton-model predictions for the two-photon exchange contribution to A_y for protons and neutrons in DIS. The first, by A. Afanasev *et al.* [11] assumes the scattering is dominated by two-photon exchange with a single quark and predicts $A_y^n \sim 10^{-4}$ at $x \sim 0.3$ and $Q^2 = 2.0$ GeV². In the second prediction, A. Metz *et al.* [12] assume the asymmetry is dominated by the process where one of the photons couples to an active quark and the other couples to a quark in the spectator di-quark system. When the interaction with the di-quark system is modeled using input from the Sivers distributions from semi-inclusive DIS [17, 18], they predict $A_y^n \sim -10^{-2}$ at the kinematics of our experiment. For consistency with our sign convention, the asymmetries in Ref. [12] have been multiplied by -1 .

This paper presents the results of Jefferson Lab experiment E07-013, which was a measurement of the neutron SSA, A_y^n , in DIS. The ϕ_S -dependent asymmetries were measured using inclusive scattering of unpolarized electrons from a ³He target polarized either vertically ($\phi_S \sim \pm 90^\circ$) or transversely ($\phi_S \sim 0^\circ, 180^\circ$) in the lab frame. A_y was obtained by fitting the ϕ_S dependence according to Eqn. (3). The nuclear ground state of ³He is dominated by the configuration in which the spins of two protons are anti-aligned, which means that the spin is mostly carried by the neutron, effectively providing a polarized neutron target.

An electron beam with energy 5.889 GeV and average current $12 \mu\text{A}$ was incident on polarized ³He gas with density ~ 10 amg contained in a 40 cm-long cylindrical aluminosilicate glass cell. The beam was rastered in a 3×3 mm² pattern to reduce the possibility of cell rupture and localized de-polarization. Polarization of the ³He nuclei was achieved via Spin-Exchange Optical Pumping (SEOP) with a hybrid alkali-metal mixture of Rb and K [19]. The polarization direction was reversed ev-

ery 20 minutes using adiabatic fast passage nuclear magnetic resonance (NMR). With each spin-flip, the NMR signals were used to measure the relative polarization. Absolute calibration was done periodically throughout the run using electron paramagnetic resonance [20]. The average polarization was 55% with a 5% relative uncertainty. The total luminosity downstream of the target was measured during each 20-minute target polarization state using eight Lucite/PMT detectors placed symmetrically around the beam line. The average luminosity asymmetry for the experiment was $(38 \pm 12) \times 10^{-6}$ which is negligible compared to our measured raw asymmetries of $\sim 10^{-3}$.

Scattered electrons were detected using the Hall A BigBite detector package [21] at $+30^\circ$ (beam-right) and the left Hall A High Resolution Spectrometer (LHRS) at -16° [22]. The BigBite package includes a dipole magnet for momentum separation, three sets of multi-wire drift chambers for track reconstruction, and a lead-glass electromagnetic calorimeter for particle identification (PID) with pre-shower and shower layers sandwiching a scintillator plane for providing timing information. The useful momentum coverage of BigBite was $0.6 < p < 2.5$ GeV with an average solid angle acceptance of 64 msr. The corresponding ϕ_S coverage is $\sim 60^\circ$ for each target polarization configuration. The LHRS consists of two sets of drift chambers for tracking, two scintillator planes for the trigger, and gas Cherenkov and lead-glass shower detectors for PID. The central momentum of the LHRS was 2.35 GeV with a momentum coverage of $\pm 4.5\%$. The solid angle acceptance was ~ 6 msr with $\sim 7^\circ$ ϕ_S coverage. Optics for both detectors were calibrated using elastic e^- scattering from hydrogen and multi-foil carbon targets. Angular reconstruction in both detectors was calibrated using a sieve slit placed in front of each spectrometer. The angular resolution in BigBite was < 10 mrad and the resolution of the reconstructed momentum was $< 1\%$.

Electron PID in BigBite began at the trigger level, which required the sum of the pre-shower and shower signals to be above a chosen threshold. Events with poor track reconstruction, tracks near the edges of the acceptance, and data that could be affected by beam trips were removed. Additional cuts included particle charge, reconstructed particle momentum, reconstructed vertex, energy deposited in the pre-shower detector ($E_{ps} > 200$ MeV), and a cut on the ratio of reconstructed energy to reconstructed momentum (E/p). The LHRS cuts were similar and included cuts on the reconstructed vertex, Cherenkov amplitude, and an E/p cut. The data from BigBite covered $0.17 < x < 0.65$ and were divided into five bins in W . The LHRS data was analyzed as a single kinematic point ($x = 0.16, W = 2.54$ GeV).

Events from three triggers taken simultaneously were used in the BigBite analysis. They are T1, proportional to the total energy deposited in the calorimeter, T6,

Detector	W GeV	x	Q^2 GeV ²	$A_y^{3\text{He}} \pm (\text{stat}) \pm (\text{sys})$ ($\times 10^{-3}$)	$A_y^n \pm (\text{stat}) \pm (\text{sys})$ ($\times 10^{-2}$)	Pair-produced background contamination (%)
BigBite	1.72	0.65	3.98	$-0.85 \pm 2.79 \pm 0.53$	$-0.55 \pm 1.81 \pm 0.36$	1.0 ± 0.8
BigBite	2.17	0.46	3.24	$-6.28 \pm 2.51 \pm 0.88$	$-3.87 \pm 1.55 \pm 0.58$	3.1 ± 1.1
BigBite	2.46	0.34	2.65	$-8.14 \pm 1.99 \pm 1.05$	$-3.89 \pm 0.96 \pm 0.53$	9.5 ± 2.0
BigBite	2.70	0.24	2.08	$-2.25 \pm 2.45 \pm 1.46$	$-1.08 \pm 1.18 \pm 0.69$	22.0 ± 4.5
BigBite	2.89	0.17	1.58	$-8.34 \pm 4.35 \pm 5.33$	$-3.84 \pm 2.00 \pm 2.42$	48 ± 10
LHRS	2.54	0.16	1.05	$-1.57 \pm 0.99 \pm 0.2$	$-0.64 \pm 0.41 \pm 0.09$	1.3 ± 0.05

TABLE I. Kinematics and results for neutron asymmetries with statistical and systematic uncertainties. The BigBite spectrometer was set at a fixed angle and central momentum and data were divided into the five kinematic bins. The final column shows measured contaminations from pair-produced electrons.

which is the same as T1 but with higher discriminator threshold, and T2, coincidence between a gas Cherenkov detector and T6. Prescale factors ranging from 2100 to 3100, 61 to 410, and 350 to 780 were used for T1, T2 and T6, respectively. Because the background rate from the Cherenkov detector was extremely high, the T2 trigger is functionally the same as the T6 trigger. Information from the Cherenkov detector was not used in this analysis. In the final dataset, T6 contributes to more than 80% of the data while T2 is about 12% and T1 is less than 8%.

Raw asymmetries for each data bin were formed as

$$A_{raw}^{e^-}(\phi_S) = \frac{1}{P_{target}} \frac{Y_{raw}^{\uparrow}(\phi_S) - Y_{raw}^{\downarrow}(\phi_S + \pi)}{Y_{raw}^{\uparrow}(\phi_S) + Y_{raw}^{\downarrow}(\phi_S + \pi)} \quad (4)$$

where the raw yields, $Y_{raw}^{\uparrow(\downarrow)}$, are the number of particles, N , observed in the target spin “up” (“down”) state that pass all data cuts for electrons, normalized by accumulated charge, Q , and DAQ livetime, LT :

$$Y_{raw}^{\uparrow(\downarrow)} = \frac{N_{raw}^{\uparrow(\downarrow)}}{Q^{\uparrow(\downarrow)} \cdot LT^{\uparrow(\downarrow)}} = \frac{N_{e^-}^{\uparrow(\downarrow)} + N_{\pi^-}^{\uparrow(\downarrow)} + N_{e^+}^{\uparrow(\downarrow)}}{Q^{\uparrow(\downarrow)} \cdot LT^{\uparrow(\downarrow)}}. \quad (5)$$

The terms N_{π^-} and N_{e^+} represent pion and pair-produced electron backgrounds that pass the good-electron cuts and P_{target} is the target polarization. The ϕ_S angle is defined for the spin up state, and changed by 180° ($\phi_S + \pi$) when the target spin was flipped.

The dominant background passing the data cuts in BigBite were photo-induced electron-positron pairs. The positrons were cut from the data by requiring particles with negative charge. However, the pair-produced electrons are indistinguishable from the desired DIS electrons. A direct measurement of the pair-produced electron contamination was made by reversing the polarity of the BigBite magnet and calculating the positron yield under conditions identical to the normal data collection. Since photons are mostly produced from neutral pion decay, the contamination decreased with increasing momentum, see Table I. This also explains why this type of background in the LHRS (central momentum of 2.35 GeV) is negligible. Negative pions were also a source of contamination. Their contributions to the BigBite data

were accounted for by fitting the pre-shower energy spectrum. Likewise, the positron data sample was contaminated by positive pions. The positive pion contamination was estimated based on the negative pion contamination. A GEANT-based Monte Carlo simulation of the BigBite spectrometer was used to study the differences between the π^+ and π^- contaminations. Data from the LHRS were relatively free of background contamination due to the choice of kinematics and exceptional PID.

Due to the large acceptance of the BigBite spectrometer, asymmetries for each type of background particle (A^{π^-} , $A_{raw}^{e^+}$, and A^{π^+}) were obtained from the data in the same way as $A_{raw}^{e^-}$ but with different selection cuts: i) positrons were selected using the same cuts as electrons except for the particle charge; ii) pions were selected using the same cuts as electrons/positrons except for requiring a pre-shower energy deposition under 150 MeV. Corrections were made to the asymmetry via:

$$A^{e^-} = \frac{A_{raw}^{e^-} - f_1 A^{\pi^-} - f_4 (1 - f_3) \frac{A_{raw}^{e^+} - f_5 A^{\pi^+}}{1 - f_5}}{1 - f_1 - f_4 (1 - f_3)}, \quad (6)$$

where the coefficients, f_i , give the fractions of mis-identified particles and are defined as:

$$\begin{aligned} f_1 &= Y_{neg}^{\pi^-} / (Y_{neg}^{e^-} + Y_{neg}^{\pi^-}) \\ f_3 &= Y_{pos}^{\pi^+} / (Y_{pos}^{e^+} + Y_{pos}^{\pi^+}) \\ f_4 &= (Y_{pos}^{e^+} + Y_{pos}^{\pi^+}) / (Y_{neg}^{e^-} + Y_{neg}^{\pi^-}) \\ f_5 &= Y_{neg}^{\pi^+} / (Y_{neg}^{e^+} + Y_{neg}^{\pi^+}). \end{aligned} \quad (7)$$

The *pos* and *neg* subscripts indicate the polarity of the BigBite magnet (standard running conditions are *neg*). The f_5 were estimated based on f_3 . Further information on these background corrections is provided in the appendix.

A small quantity of unpolarized N_2 was used in the ^3He target-cell to improve the efficiency of the optical pumping. The asymmetry was corrected by a dilution factor defined as:

$$\eta_{N_2} \equiv \frac{1}{1 + \left(\frac{\rho_{N_2}}{\rho_{^3\text{He}}} \right) \left(\frac{\sigma_{N_2}}{\sigma_{^3\text{He}}} \right)} \quad (8)$$

where ρ are the densities and σ are the unpolarized cross-sections for each gas. The ratio of densities is taken from the target cell filling data. The cross-section ratio is determined experimentally by inelastic scattering from a reference cell filled with known densities of either N_2 or 3He . The dilution factors for BigBite measured for T1 and T6 triggers agree with each other. The final dilution was determined by combining results from T1 and T6 according to their statistical uncertainties, giving $\eta \sim 0.9$ for all kinematics with an uncertainty of $\sim 2\%$. The dilution factor for the LHRS was determined to be 0.851 ± 0.018 . The 3He asymmetries from BigBite T1, T2 and T6 triggers were extracted independently and were consistent with each other within the statistical uncertainties for each bin. The final 3He asymmetries were obtained by combining the results from the T1, T2 and T6 asymmetries according to their statistical uncertainties.

Neutron asymmetries were obtained from the 3He asymmetries using the effective polarizations of the proton and neutron in polarized 3He using [23],

$$A_y^{^3He} = (1 - f_p)P_n A_y^n + f_p P_p A_y^p \quad (9)$$

Here, $P_n = 0.86^{+0.036}_{-0.02}$ ($P_p = -0.028^{+0.009}_{-0.004}$) is the effective neutron (proton) polarization [24].

The proton dilutions of 3He for BigBite, $f_p = \frac{2\sigma_p}{\sigma_{^3He}}$, were measured for the T1 and T6 triggers using the yields from unpolarized hydrogen and 3He targets and are consistent with each other. The final dilutions, which varied between 0.75 – 0.82, with uncertainties of 0.02 – 0.08, were determined by combining the T1 and T6 results according to their statistical uncertainties. Neutron asymmetries were calculated separately for each trigger type and combined according to their statistical uncertainties. The proton dilution for the LHRS was 0.715 ± 0.007 . A value of $A_y^p = (0 \pm 3) \times 10^{-3}$ was used in Eqn. (9) based on the HERMES measurements [16]. External radiative corrections were applied to both the BigBite and LHRS data using a Monte Carlo simulation that included detailed modeling of geometry and material in the target and spectrometers. No correction was made on the asymmetries since the radiative corrections to the two-photon exchange process are not yet available and the phase space of this measurement is limited.

The dominant systematic uncertainty for BigBite is from background contamination, the largest of which is from pair-produced electrons, see Table I. The π^- contamination in the T6 triggers ranges from 0.5 to 2.0% (rel.) from the lowest to highest W bin, respectively. The uncertainties on the contamination are $\sim 0.5\%$, which were estimated using the difference between information from the Monte Carlo simulation and contamination estimation based on data. Further details about these corrections for the other two triggers (T1 and T2) can be found in the appendix. The uncertainties associated with backgrounds contribute to both the asymmetries

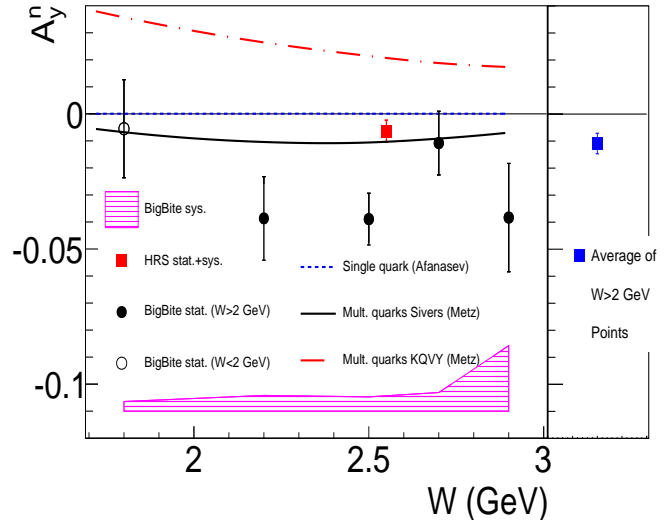


FIG. 3. Neutron asymmetry results (color online). **Left panel:** Solid black data points are DIS data ($W > 2$ GeV) from the BigBite spectrometer; open circle has $W = 1.72$ GeV. BigBite data points show statistical uncertainties with systematic uncertainties indicated by the lower solid band. The square point is the LHRS data with combined statistical and systematic uncertainties. The dotted curve near zero (positive) is the calculation by A. Afanasev *et al.* [11], The solid and dot-dashed curves are calculations by A. Metz *et al.* [12] (multiplied by -1). **Right panel:** The average measured asymmetry for the DIS data with combined systematic and statistical uncertainties.

and dilution factors. The final results were extracted taking into account the full correlation of these uncertainties. Other BigBite systematic uncertainties include the detector acceptance (1.2×10^{-4}), detector response drift (9×10^{-5}), and livetime asymmetry (6×10^{-5}). For the LHRS, systematic uncertainties include the livetime asymmetry (6×10^{-5}) and tracking efficiency (7×10^{-5}). The correction to the LHRS asymmetry due to pair-produced electrons is 1.56×10^{-4} with a 100% relative uncertainty. Systematic uncertainties from the polarized target include target polarization and misalignment (5%), and luminosity fluctuations (1.2×10^{-5}).

The 3He and neutron results are presented in Table I along with the pair-produced electron contamination. Neutron results are shown in Fig. 3. The asymmetry is generally negative and non-zero across the measured kinematic range. At the largest value of W , the systematic uncertainty is quite large due to the uncertainty in the pair-produced electron contamination. In order to evaluate how much the data disfavors the zero-asymmetry hypothesis in the DIS region, the average asymmetry was calculated for the data with $W > 2.0$ GeV. Because the systematic uncertainties of the BigBite points are mostly due to background contamination,

they were assumed to be fully correlated, and uncorrelated with the LHRS point. The final average neutron asymmetry in the DIS region and its total experimental uncertainty are determined to be $(-1.09 \pm 0.38) \times 10^{-2}$, which is non-zero at the 2.89σ level. The data are in good agreement with the two-photon exchange prediction by A. Metz *et al.* [12], $A_y^n \sim -10^{-2}$, that uses model input from the semi-inclusive DIS Sivers distribution.

We have presented the first measurements of the neutron target-normal SSA, A_y^n , in the DIS region using a polarized ^3He target. Because A_y must be zero at Born-level its measurement is a valuable laboratory for studying two-photon exchange and the dynamics of the nucleon beyond the simple quark-parton model. Further measurements for both proton and neutron with higher precision over a broader kinematic range are necessary to gain a deeper understanding of the role of two-photon exchange in nucleon structure studies.

We acknowledge the outstanding support of the Jefferson Lab Hall A technical staff and Accelerator Division in accomplishing this experiment. We thank A. Afanasev, C. Weiss and A. Metz for their valuable theoretical guidance. This work was supported in part by the U.S. National Science Foundation, the UK Science and Technology Facilities Council, the U.S. Department of Energy and by DOE contract DE-AC05-06OR23177, under which Jefferson Science Associates, LLC operates the Thomas Jefferson National Accelerator Facility.

APPENDIX

The tables in this appendix show the values used for the corrections in equations (5) and (6). Here, we use the notation $f_4 = Y_2/Y_1$, $f_3 = Y_3/Y_2$, and $f_5 = C \cdot Y_3/Y_2$, with $C = 1.8 \pm 0.4$. The triggers are T1: proportional to the total energy deposited in the electromagnetic calorimeter, T2: coincidence between gas Cherenkov and calorimeter energy deposited, T6: same as T1 but with higher discriminator threshold. The data from the three triggers were corrected for background and combined. Here, Y_1 , Y_2 , Y_3 are yields (events normalized by accumulated charge and detector livetime). The unit is events/ μC .

-
- * Corresponding author: tdaver@wm.edu
† Deceased
- [1] J. Arrington, Phys. Rev. **C68**, 034325 (2003).
 - [2] J. Arrington, P. Blunden, and W. Melnitchouk, Prog. Part. Nucl. Phys. **66**, 782 (2011), arXiv:1105.0951 [nucl-th].
 - [3] M. Christy *et al.* (E94110 Collaboration), Phys. Rev. **C70**, 015206 (2004), arXiv:nucl-ex/0401030 [nucl-ex].
 - [4] I. Qattan, J. Arrington, R. Segel, X. Zheng, K. Aniol, *et al.*, Phys. Rev. Lett. **94**, 142301 (2005), arXiv:nucl-ex/0410010 [nucl-ex].
 - [5] A. Puckett, E. Brash, O. Gayou, M. Jones, L. Pentchev, *et al.*, Phys. Rev. **C85**, 045203 (2012), arXiv:1102.5737 [nucl-ex].
 - [6] P. G. Blunden, W. Melnitchouk, and J. A. Tjon, Phys. Rev. Lett. **91**, 142304 (2003).
 - [7] Y. C. Chen, A. Afanasev, S. J. Brodsky, C. E. Carlson, and M. Vanderhaeghen, Phys. Rev. Lett. **93**, 122301 (2004), arXiv:hep-ph/0403058 [hep-ph].
 - [8] C. E. Carlson and M. Vanderhaeghen, Annu. Rev. Nucl. Part. Sci. **57**, 171 (2007).
 - [9] N. Christ and T. D. Lee, Phys. Rev. **143**, 1310 (1966).
 - [10] R. N. Cahn and Y. S. Tsai, Phys. Rev. **D2**, 870 (1970).
 - [11] A. Afanasev, M. Strikman, and C. Weiss, Phys. Rev. **D77**, 014028 (2008).
 - [12] A. Metz *et al.*, Phys. Rev. **D86**, 094039 (2012).
 - [13] M. Schlegel, Phys. Rev. **D87**, 034006 (2013), arXiv:1211.3579 [hep-ph].
 - [14] J. R. Chen *et al.*, Phys. Rev. Lett. **21**, 1279 (1968).
 - [15] S. Rock *et al.*, Phys. Rev. Lett. **24**, 748 (1970).
 - [16] A. Airapetian *et al.*, Phys. Lett. **B682**, 351 (2010).
 - [17] M. Alekseev *et al.* (COMPASS Collaboration), Phys. Lett. **B673**, 127 (2009), arXiv:0802.2160 [hep-ex].
 - [18] A. Airapetian *et al.* (HERMES Collaboration), Phys. Rev. Lett. **103**, 152002 (2009), arXiv:0906.3918 [hep-ex].
 - [19] E. Babcock *et al.*, Phys. Rev. Lett. **91**, 123003 (2003).
 - [20] M. V. Romalis and G. D. Cates, Phys. Rev. **A58**, 3004 (1998).
 - [21] M. Mihovilovic, K. Allada, B. Anderson, J. Annand, T. Averett, *et al.*, Nucl. Instrum. Meth. **A686**, 20 (2012), arXiv:1201.1442 [nucl-ex].
 - [22] J. Alcorn *et al.*, Nucl. Instrum. Meth. **A522**, 294 (2004).
 - [23] S. Scopetta, Phys. Rev. **D75**, 054005 (2007).
 - [24] X. Zheng *et al.*, Phys. Rev. **C70**, 065207 (2004).

Bin no.	T1	T1 stat. rel.	T1 sys. rel.	T2	T2 stat. rel.	T2 sys. rel.	T6	T6 stat. rel.	T6 sys. rel.
1	0.0071	0.069	1	0.0034	0.14	1	0.0038	0.031	1
2	0.019	0.031	0.6	0.008	0.053	0.6	0.0076	0.016	0.6
3	0.044	0.013	0.35	0.014	0.027	0.35	0.013	0.0082	0.35
4	0.084	0.008	0.35	0.016	0.021	0.35	0.016	0.0062	0.35
5	0.11	0.006	0.35	0.020	0.018	0.35	0.023	0.0047	0.35

TABLE II. Tabulated f_1 and its errors.

Bin no.	T1	T1 stat. rel.	T1 sys. rel.	T2	T2 stat. rel.	T2 sys. rel.	T6	T6 stat. rel.	T6 sys. rel.
1	3.90	0.0208	0	2.74	0.00894	0	3.76	0.00698	0
2	6.13	0.0166	0	4.31	0.00712	0	5.89	0.00557	0
3	12.8	0.0115	0	8.73	0.00500	0	12.0	0.00389	0
4	16.3	0.0102	0	9.65	0.00475	0	13.3	0.00370	0
5	32.5	0.00721	0	11.2	0.00440	0	15.7	0.00340	0

TABLE III. Tabulated Y_1 and its errors.

Bin no.	T1	T1 stat. rel.	T1 sys. rel.	T2	T2 stat. rel.	T2 sys. rel.	T6	T6 stat. rel.	T6 sys. rel.
1	0.0310	1.00	0.15	0.065	0.123	0.15	0.0645	0.151	0.15
2	0.232	0.378	0.15	0.191	0.0718	0.15	0.259	0.0756	0.15
3	2.29	0.119	0.15	1.00	0.0313	0.15	1.43	0.0321	0.15
4	5.64	0.0761	0.15	2.32	0.0206	0.15	3.37	0.0209	0.15
5	20.9	0.0394	0.15	5.82	0.0130	0.15	8.24	0.0134	0.15

TABLE IV. Tabulated Y_2 and its errors.

Bin no.	T1	T1 stat. rel.	T1 sys. rel.	T2	T2 stat. rel.	T2 sys. rel.	T6	T6 stat. rel.	T6 sys. rel.
1	0.0310	0.185	1	0.0154	0.0734	1	0.0239	0.0718	1
2	0.173	0.125	0.6	0.0569	0.0394	0.6	0.0736	0.0390	0.6
3	0.945	0.0506	0.35	0.224	0.0191	0.35	0.291	0.0185	0.35
4	2.42	0.0298	0.35	0.312	0.0143	0.35	0.403	0.0141	0.35
5	7.03	0.0166	0.35	0.530	0.00937	0.35	0.905	0.00858	0.35

TABLE V. Tabulated Y_3 and its errors.

Setup	Bin 1	Bin 2	Bin 3	Bin 4	Bin 5
T1 electron	0.0132	0.00930	-0.000216	0.0163	-0.00392
T1 electron abs. err.	0.0104	0.00837	0.00578	0.00515	0.00369
T2 electron	-0.00429	0.00161	0.00723	0.0000208	-0.00200
T2 electron abs. err.	0.00778	0.00619	0.00434	0.00412	0.00381
T6 electron	0.000968	0.00524	0.00309	-0.00343	-0.00574
T6 electron abs. err.	0.00259	0.00211	0.00149	0.00145	0.00141
T1 positron	-0.0198	-0.0742	-0.0449	-0.0160	-0.0281
T1 positron abs. err.	0.0841	0.0405	0.0171	0.0110	0.0064
T2 positron	0.00812	0.0239	-0.0372	-0.0103	-0.0218
T2 positron abs. err.	0.0674	0.0343	0.0154	0.0103	0.00709
T6 positron	0.0329	-0.00966	-0.0229	-0.0217	-0.0188
T6 positron abs. err.	0.0228	0.01182	0.00537	0.00364	0.00258
T1 π^-	-0.0402	-0.0204	-0.00313	0.0251	0.0201
T1 π^- abs. err.	0.01688	0.00921	0.00427	0.00293	0.00189
T2 π^-	-0.0495	-0.0479	0.0138	0.0394	0.0237
T2 π^- abs. err.	0.0305	0.0175	0.00886	0.00672	0.00490
T6 π^-	-0.0735	-0.0391	-0.00061	0.0255	0.0185
T6 π^- abs. err.	0.00979	0.00565	0.00287	0.00216	0.00157
T1 π^+	-0.00313	0.0148	-0.00276	-0.0185	-0.00876
T1 π^+ abs. err.	0.0364	0.0165	0.00709	0.00480	0.00341
T2 π^+	0.0576	-0.00439	0.00625	-0.0020	-0.0181
T2 π^+ abs. err.	0.0401	0.0218	0.0123	0.0125	0.0150
T6 π^+	0.00939	-0.00534	-0.0156	-0.0189	-0.0165
T6 π^+ abs. err.	0.0131	0.00716	0.0042	0.00428	0.00566

TABLE VI. Raw asymmetries for each type of particle, corrected for beam charge and livetime.